Progress in Additive Manufacturing
https://doi.org/10.1007/s40964-025-01271-6

RESEARCH

Quasistatic mechanical properties of Inconel 718 triply periodic minimal surfaces: effect of standard heat treatments on compressive strength and energy absorption

Mobin Majeed[1] · **Rong Situ**[1]

Received: 23 April 2025 / Accepted: 19 July 2025

Abstract
Triply periodic minimal surfaces (TPMS), structures fabricated from Inconel 718 (In718) via selective laser melting (SLM), found their potential applications in the aviation and energy industries owing to their excellent anticorrosive properties and thermal stability. However, the SLM process induces micro-segregation, anisotropic mechanical properties, and detrimental phases (Laves, δ) which degrade its mechanical properties. Although heat treatment has shown promising results for bulk In718 material, its impact on TPMS structures has received very limited attention. This research investigates the impact of standard heat treatments, including stress relieving (SR), homogenization plus ageing (HSA), and direct ageing (DA), on the properties of diamond and gyroid TPMS structures. The quasistatic compression tests were conducted in an Instron machine, and material characterisation was conducted in Scanning Electron Microscopy (SEM) and X-ray diffraction (XRD). HSA treatment has led to maximum improvement; the compressive strength and yield strength of diamond TPMS were improved by 58.55% and 93.5% respectively, due to the precipitation of strengthening phases (γ' and γ'') and dissolution of detrimental phases. HSA and DA treatments led to stretch dominated deformation and higher energy absorption capacity. Conversely SR treatment has shown bending dominated deformation behaviour and degraded mechanical properties in contrast to the previous studies on tensile samples.

Keywords Selective laser melting · In718 · Triply periodic minimal surfaces · Heat treatment · Mechanical properties

1 Introduction

1.1 TPMS structures

Lattice structures are cellular materials formed by periodic arrangements of struts of plates in three-dimensional space [1, 2]. They are broadly investigated due to their superior mechanical, thermal, electrical properties in combination to light weight [3]. Numerous types of lattice structures have been fabricated such as BCC, HCP, FCC, HCP, honeycomb, stochastic etc. Their applications range from aerospace, energy, automotive, biomedical implants, sandwich panels etc. Recently, a category of lattice structures known as triply periodic minimal surfaces (TPMS) have achieved great attention ascribed to their easy manufacturing, superior specific strength, stiffness, energy absorption, better heat transfer control and biocompatibility [4]. Its surfaces have zero mean curvature which facilitates uniform stress distribution, and self-support during additive (AM) process [5]. They have proven excellent compressive properties, owing to their unique topology, smooth surface which provides uniform stress distribution and stable deformation [6].

1.2 Classification of TPMS structures

TPMS structures can be classified into skeletal-based and sheet-based depending upon the morphology of unit cell, whilst the latter is preferred due to its superior mechanical properties [7]. Complex structure of TPMS structures make it very challenging to produce with conventional manufacturing methods. Only with the advent of AM the fabrication of these structures is commercially feasible. Selective laser melting (SLM) is the prominent AM technique to fabricate

✉ Rong Situ
rong.situ@jcu.edu.au

Mobin Majeed
mobin.majeed@my.jcu.edu.au

[1] James Cook University, Townsville, Australia

Published online: 28 July 2025

TPMS structures from various metals including AlSi10Mg, 316 L, CoCr, and titanium alloys [8–10]. Unique topology of TPMS structures is anticipated to provide promising properties in defence applications, energy sector, aerospace and automotive sector [11]. However, the other characteristics such as base material and relative density also considerably impact their properties.

1.3 Manufacturing and mechanical properties of TPMS structures

Relative density, topology, base material and heat treatment are some of the prominent parameters that govern the mechanical performance of TPMS structures. Therefore, it is necessary to relate these design parameters to the mechanical behaviour of TPMS structures. Ravichandra et al. [8] investigated the compressive and tensile properties of five popular Ti6Al4V TPMS structures and noted a substantial difference in properties of each TPMS due to their topology. Fisher TPMS demonstrated top yield strength, followed by diamond, and gyroid was the weakest. Another study investigated the influence of heat treatment on the compressive properties of uniform and graded 316L TPMS structures and claimed that despite the same relative density, they had different mechanical properties and different reaction to heat treatment [12]. Ahmed et al. [13] found considerable variation in mechanical properties of TPMS structures fabricated from Ti64, Inconel (In718), and 316L alloy, due to difference in strength and microstructure of the base material. Feng et al. [14] tested diamond and gyroid TPMS structures in compression and found that a linear relationship exists between mechanical properties and relative density of TPMS structures. Elastic modulus, yield strength and energy absorption were strictly increasing by raising the relative density.

1.4 SLM microstructure of In718

In718 is a Ni-based precipitation hardened superalloy widely applied in the aerospace, energy, nuclear, gas, and oil industries; however, SLM In718 possesses a non-equilibrium microstructure [15–17]. In718 alloy possesses some unique characteristics such as high mechanical strength, good weldability, and the ability to operate in harsh corrosive environments at high temperatures up to ~ 700 °C in aerospace and energy industries [18–20]. SLM is generally employed to fabricate hard to machine In718 complex structures [21] for these applications due to its design flexibility. In718 consists of Ni-based γ matrix with γ' and γ'' strengthening phases, carbides, brittle Laves phases, and δ phases; details are illustrated in Table 1.

The SLM In718 microstructure significantly differs from cast or wrought fabricated alloys [24]. The non-equilibrium microstructure of In718 in SLM evolves from rapid cooling (10^3–10^7 K/s), high solidification rates, and cyclic heating cooling [25]. This causes micro-segregation of elements, higher amount of precipitation of detrimental phases such as Laves and δ, large columnar grains, and anisotropic mechanical properties [26]. The detrimental phases suppress the precipitation of strengthening precipitates γ' and γ'' [27]. Therefore, the as built In718 material microstructure needs to be improved by post processing to gain considerable strength. The only way to tailor the microstructure of SLM In718 alloy is by applying a suitable post heat treatment procedure.

Table 1 Chemical and lattice parameters of In718 precipitates [22, 23]

Phase	Chemical composition	Crystal structure
γ	Ni	FCC
γ'	Ni3(Al,Ti, Nb)	FCC(LI_2)
γ''	Ni_3Nb	BCT (DO_{22})
Laves	$(Ni,Cr,Fe)_2(Nb,Mo,Ti)$	HCP
δ	$Ni_3(Nb, Ti)$	Orthorhombic(DO_a)
Carbide	(N,Ti)(C,N)	Cubic

1.5 Heat treatment of SLM In718 TPMS structures

The microstructure of In718 produced via SLM In718 is highly influenced by parameters of subsequent heat treatment, which in turn critically impact its mechanical properties. Researchers have proposed heat treatment parameters based on the dissolution of undesirable phases such as Laves and δ, and the precipitation of γ' and γ'' strengthening phases. Notably, these heat treatments were developed for post processing of In718 alloy obtained from conventional manufacturing methods. Nonetheless, individual or combined heat treatment are used to tailor the SLM In718 mechanical properties. Traditional and standard heat treatments of SLM bulk In718 involves:

- Solution treatment/ageing (SA),
- Direct ageing (DA),
- Homogenization,
- Stress relieving (SR),
- Full heat treatment (FHT), and
- Hot isostatic pressing (HIP) [28–30].

FHT was especially designed for the additively manufactured In718 alloys. Zhao et al. [31] observed that homogenization treatment at 1180 °C for 1 h completely recrystallized the grains and improved the isotropic tensile properties of In718, whilst heat treatment at 1065 °C for 2 h failed to do so. Babamiri et al. [32] evaluated the compressive

mechanical properties of bulk In718 treated by SR, HIP, and SA. The SR, SA, and HIP improved the compressive strength by 44%, 97%, and 50%, respectively. Schroder et al. [22] has evaluated the tensile mechanical properties of SLM In718 after DA and FHT treatments according to ASTM F3301. Although FHT is recommended for SLM In718 alloys, the mechanical properties of simple two step DA treated samples were comparable to FHT samples. Moreover, the tensile strength of DA In718 was achieving the cast and wrought standards. Hence, it is possible to exclude the HIP and FHT from recommended heat treatment methods for additively manufactured In718 and still achieve properties comparable to wrought and cast standards. For this reason, this study includes DA, SR, and homogenization heat treatments to save excess cost and time involved.

1.6 Heat treatment method for TPMS structures

As discussed above three heat treatments are considered in this study for specific reason to investigate their impact on TPMS structures based on previous studies [22, 33]. Their corresponding parameters are listed in AIM.

Substantial research has explored the mechanical behaviour of TPMS structures based on its topology, strain rate and relative density, ignoring the role of microstructure in governing TPMS properties. However, for advanced applications such as aerospace and energy sectors, the as built TPMS structures must be properly heat treated.

Previous studies have shown that heat treatment significantly improves the microstructure and mechanical properties of bulk In718 material [34–36]. Nevertheless, the impact of TPMS structures to these heat treatments is unexplored. Owing to the complex internal structure of TPMS compared to bulk material, it is unlikely that the response of TPMS structures under these heat treatments will be identical.

This study hypothesises that, analogous to the enhancements made in the bulk In718 material, the mechanical performance of TPMS structures can also be substantially improved. Accordingly, this study investigates the influence of three standard heat treatments, DA, SR and HSA, on the microstructure and compressive mechanical properties of TPMS structures with the following objectives. (However, these heat treatments were not optimised for TPMS structures as the behaviour of these treatments in relation to TPMS is still not clear.)

- To compare the impact of mentioned heat treatments on microstructure evolution of TPMS structures.
- To examine the response of heat treatment on TPMS topology and relative density.
- To investigate the impact of heat treatment on stress strain behaviour, deformation mechanism, energy absorption characteristics, and densification strain of TPMS structures.

The microstructure of In718 was examined using a scanning electron microscope (SEM), and the mechanical properties of TPMS were evaluated following standard compression testing. This study highlights new insight into the compressive properties and energy absorption characteristics of TPMS structures following the standard heat treatments. Furthermore, the study identified a different behaviour of heat treatment on energy absorption properties and densification strain. In addition, an unreported contradictory behaviour of SR treatment on mechanical properties was highlighted, which is not aligned with prior research.

These heat treatments are intended to compare the effect of In718 precipitates such as δ, Laves, strengthening phases γ' and γ'', on mechanical properties of TPMS structures:

- ASTM F3301 recommends SR at 1065 °C: this treatment is above the dissolution temperature and intended to dissolve δ phase but retains some Laves phases.
- DA as per AMS 2774: this treatment is expected to precipitate γ' and γ'' strengthening phases but retain other detrimental phases.
- Homogenization and ageing treatment (HSA): this treatment completely recrystallizes the microstructure, dissolves Nb and brittle phases including Laves and δ [37]. A solution cycle (980°C) as per AMS 2774 is added following homogenization cycle to precipitate δ-phase in intragranular region. Lastly DA treatment cycle is added to precipitate γ' and γ'' strengthening phases (Table 2).

1.7 AIM

Substantial research has explored the mechanical behaviour of TPMS structures based on its topology, strain rate, and relative density, ignoring the role of microstructure in governing TPMS properties. However, for advanced applications such as aerospace and energy sectors, the as built TPMS structures must be properly heat treated.

Previous studies have shown that heat treatment significantly improves the microstructure and mechanical properties of bulk In718 material [34–36]. Nevertheless, the impact of TPMS structures to these heat treatments is unexplored. Owing to the complex internal structure of TPMS compared to bulk material, it is unlikely that the response of TPMS structures under these heat treatments will be identical.

This study hypothesises that, analogous to the enhancements made in the bulk In718 material, the mechanical performance of TPMS structures can also be substantially improved. Accordingly, this study investigates the

Table 2 Heat treatment parameters for TPMS structures

Heat treatment	Action of treatment	Solution temperature/hour (°C)		Ageing temperature/hour (°C)		Reference
		Cycle 1	Cycle 2	Cycle 3	Cycle 4	
As built (AB)	As fabricated microstructure					
Stress relieving (SR)	Elimination of δ phase, retain some Laves phase. Remove stresses	1065/1.5				[38]
Direct ageing (DA)	Precipitation of γ' and γ'' phase			718/18	621/10	[39]
Homogenization and solution ageing (HSA)	Recrystallisation + δ precipitation + (γ' and γ'' phase)	1080/1.5	980/1	718/8	621/10	[40]

influence of three standard heat treatments, DA, SR, and HSA, on the microstructure and compressive mechanical properties of TPMS structures with the following objectives. (However, these heat treatments were not optimised for TPMS structures as the behaviour of these treatments in relation to TPMS is still not clear.)

- To compare the impact of mentioned heat treatments on microstructure evolution of TPMS structures.
- To examine the response of heat treatment on TPMS topology and relative density.
- To investigate the impact of heat treatment on stress strain behaviour, deformation mechanism, energy absorption characteristics, and densification strain of TPMS structures.

The microstructure of In718 was examined using a scanning electron microscope (SEM), and the mechanical properties of TPMS were evaluated following standard compression testing. This study highlights new insight into the compressive properties and energy absorption characteristics of TPMS structures following the standard heat treatments. Furthermore, the study identified a different behaviour of heat treatment on energy absorption properties and densification strain. In addition, an unreported contradictory behaviour of SR treatment on mechanical properties was highlighted, which is not aligned with prior research.

2 Experimental procedure

2.1 Designing method of In718 sheet based TPMS structures

The isosurfaces of the TPMS structures were designed from their trigonometric function using the following equations:

$$f_d(x,y,z) = \cos\cos\left(\frac{2\pi}{l}x\right)\cos\cos\left(\frac{2\pi}{l}y\right)\cos\cos\left(\frac{2\pi}{l}z\right) - \sin\sin\left(\frac{2\pi}{l}x\right)\sin\sin\left(\frac{2\pi}{l}y\right)\sin\left(\frac{2\pi}{l}z\right)$$

$$f_g(x,y,z) = \sin\sin\left(\frac{2\pi}{l}x\right)\cos\cos\left(\frac{2\pi}{l}y\right) + \sin\sin\left(\frac{2\pi}{l}y\right)\cos\cos\left(\frac{2\pi}{l}z\right) + \sin\sin\left(\frac{2\pi}{l}z\right)\cos\left(\frac{2\pi}{l}x\right)$$

where $f_d(x,y,z)$ and $f_g(x,y,z)$ are isosurface odiamond and gyroid, respectively, l is the size of unit cell in three cartesian directions x, y, and z. The surface at $f(x,y,z) = 0$, is the midsurface of TPMS structure, which divides the space into two equal parts. The iso-surface of TPMS was exported from MATLAB to a CAD design package for extrusion in two directions equally. TPMS structures with two levels of relative densities (12% and 22%) and a cell size of $l = 6$ mm $\times$ 6 mm $\times$ 6 mm were designed with the sample dimension of 24 mm $\times$ 24 mm $\times$ 24 mm: containing 4-unit cells; other parameters recorded in Table 3. The TPMS structures are named according to their topology and relative density and referred with the same nomenclature in this manuscript.

2.2 Manufacturing procedure of TPMS structures

In718 TPMS structures were fabricated from gas-atomized 1n718 power, supplied by Renishaw, U.K.; chemical composition is in accordance with ASTM B637; see Table 4. The specimens were fabricated in a Renishaw AM400 machine fitted with a 400-W ytterbium fibre laser. The machine had a build-up size of 250 mm $\times$ 250 mm $\times$ 300 mm and was supplied with high purity argon gas for shielding. Optimised process parameters to achieve the high-quality are outlined in Table 5. A meander scan strategy was used for laser scanning, and laser direction was rotated by 67° between

Table 3 Details of geometrical parameters of TPMS structures

TPMS Design	Nomenclature	Heat treatment	Relative density, ρ	Weight, m [grammes]	Volume [cm^3]
Diamond	D12	AB	12.4	34.94	3.991
Diamond	D12	SR	12.4	34.62	3.991
Diamond	D12	DA	12.4	35.01	3.991
Diamond	D12	HSA	12.4	34.32	3.991
Diamond	D24	AB	22.19	43.5	5.683
Diamond	D24	SR	22.19	44.96	5.683
Diamond	D24	DA	22.19	43.64	5.683
Diamond	D24	HSA	22.19	44.70	5.683
Gyroid	G12	AB	12.36	32.82	3.998
Gyroid	G12	SR	12.36	33.27	3.998
Gyroid	G12	DA	12.36	32.61	3.998
Gyroid	G12	HSA	12.36	32.49	3.998
Gyroid	G24	AB	22.32	44.45	5.755
Gyroid	G24	SR	22.32	44.25	5.755
Gyroid	G24	DA	22.32	44.73	5.755
Gyroid	G24	HSA	22.32	44.36	5.755

*Unit cell size = 6 mm × 6mm × 6mm, Dimension = 24mm × 24mm × 24mm

Table 4 Weight percentage of elements in In718 alloy powder

Element		Ni	Cr	Nb + Ta	Mo	Ti	Co	Al	Mn	Si	Cu	C	O
ASTM B67	Min	50.0	17.0	4.75	2.80	0.65		0.20					
Wt. %	Max	55.0	21.0	5.50	3.3	1.15	1.00	0.80	0.35	0.35	0.30	0.08	
This study	Min	50.0	17.0	4.75	2.80	0.65		0.20				0.02	
	Max	55.0	21.0	5.50	3.3	1.15	1.00	0.80	0.35	0.35	0.30	0.05	

Table 5 Process parameters for SLM of In718 in this study

Laser power (W)	Exposure time	Layer thickness	Point distance	Hatch distance
200	80 µs	60 µm	70 µm	90 µm

consecutive layers during fabrication. The fabricated specimens were separated from the build plate by wire EDM and grouped for distinct heat treatments; see Fig. 1.

2.3 Microstructural analysis and property characterization

Microstructure analysis of In718 specimens were conducted in a field emission (JEOL JSM-7800F) scanning electron microscope (SEM) equipped with an X-ray spectroscopy (EDS) analysis system The SEM was operated at 15 kV, and a working distance of around 10 mm was set for maximum focus. Prior to analysis, the surface of the bulk specimens were polished with SiC papers #220-1200, followed by fine polishing with diamond and silica suspension. The specimens were also etched in ion mill IM4000 to reveal precipitates and grain boundaries in SEM.

2.4 Mechanical characterisation of In718 and property characterisation

The TPMS structures were tested on an electronic testing machine, an Instron 5980 series fitted with a maximum load cell capacity of 600 kN. The tests were performed under a constant crosshead speed of 2 mm/min, up to 70% strain, in accordance with the ISO 13314:2014 standard. Two samples were tested for each condition to maintain consistency of results. The force displacement data was recorded, and the deformation process was captured on camera. The specimens were held between the two small rectangular steel plates, which were used to position the samples in the middle of the test table. These steel plates were machined after significant scratches were observed. A more detailed description of the use of fixtures for testing can be found elsewhere [41, 42].

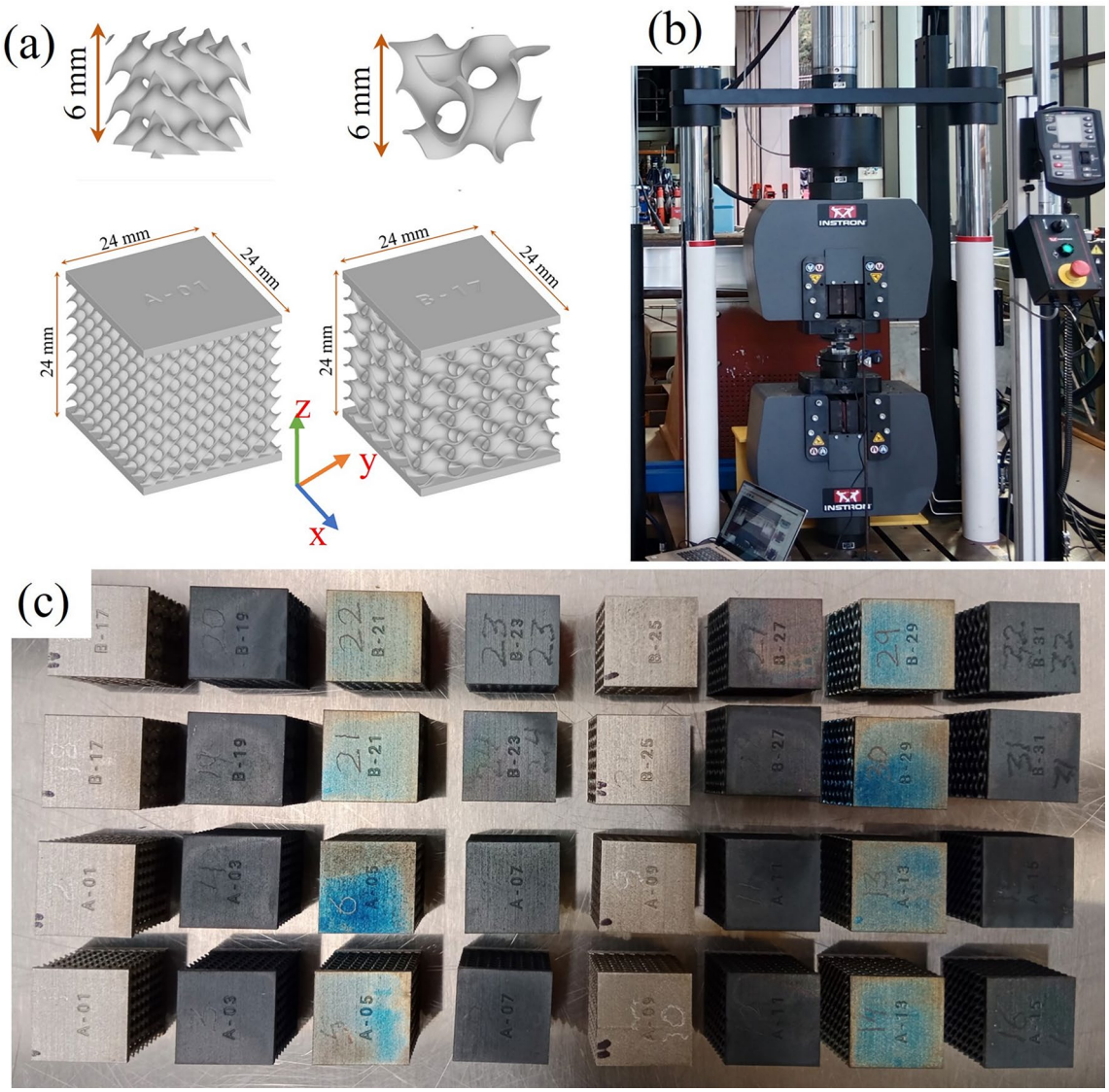

Fig. 1 **a** CAD model and fabricated TPMS structures, **b** Universal testing machine, **d** Fabricated and heat treated TPMS samples

3 Experimental results and analysis

The microstructure of TPMS structures is illustrated in Fig. 2, along both the build direction (XZ plane) and perpendicular to it (XY plane). The microstructure in the XZ plane contains elongated morphologies whose longitudinal axis appears to be inclined along the build direction, depicting directional solidification. However, in the XY plane, grains appear to be more equiaxed and randomly oriented with no specific crystallographic orientation.

3.1 Microstructure in AB condition

The microstructure of In718 in the AB condition is characterised by cellular dendritic structure and columnar grains, as depicted in Fig. 2a, b, and Fig. 3a. The dendrite formation at and inside grain boundaries is attributed to micro-segregation during solidification. The segregation of elements such as niobium (Nb), Laves, and carbide phases was revealed in the energy dispersive X-ray spectroscopy (EDS). However, typical precipitates of In718, such as δ, γ', and γ'' were not identified in the AB In718 matrix due to rapid cooling and solidification in the SLM process. The presence of the Laves phase is detrimental to the mechanical properties of In718 TPMS structures due to their brittle nature. Consequently, heat treatment was applied to suppress the micro-segregation and promote the precipitation of strengthening phases.

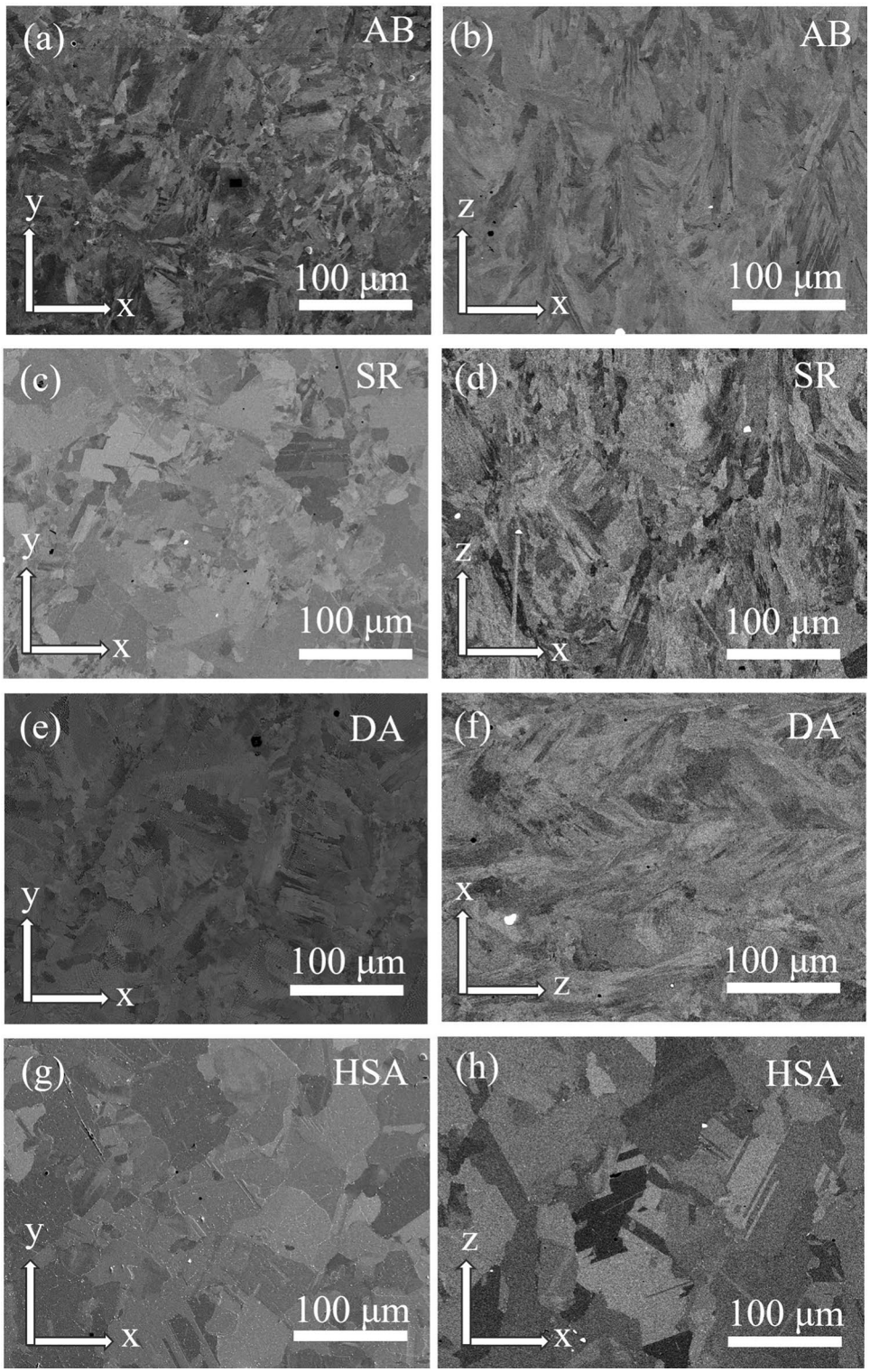

Fig. 2 SEM micrograph of In718 in different state of heat treatments **a** as built, **b** SR, **c** DA, and **d** HSA

3.2 Microstructure in SR condition

Following SR treatment, noticeable changes in grain size and morphology were recorded, as shown in Fig. 2c, and d. Nevertheless, most of the columnar morphology persisted. Laves phases were still present in the matrix in a partially dissolved state, as depicted in Fig. 3b. These partially dissolved Laves phases appear to be broken forms of long chain Laves from the AB state and were also confirmed by the EDS analysis in Fig. 4d. In addition, a high volume of carbides was also identified along the grain boundaries, as evident in Fig. 4b and supported by EDS analysis in Fig. 4e. The SR temperature

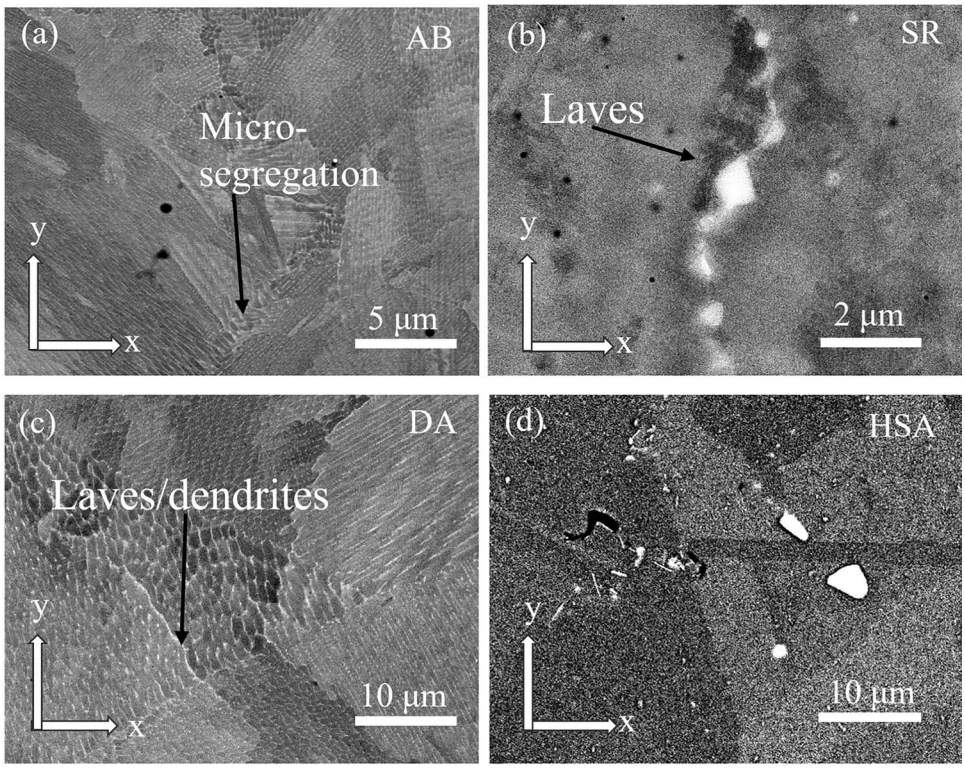

Fig. 3 SEM detailed micrograph of In718 in different state of heat treatments **a** as built, **b** SR, **c** DA, and **d** HSA

is insufficient to fully dissolve Laves phases, yet sufficient for the diffusion of Nb and other elements to facilitate carbide growth and ultimately strengthen it [43]. However, the high volume of carbides promotes crack initiation and is detrimental to the mechanical properties of material. The solvus temperature of carbides is reported to be between 1260 and 1305 °C [44]. Since the dissolution range of the δ phase is 980 °C to 1020 °C [45], they were not identified in the matrix.

3.3 Microstructure in DA condition

In the DA samples, no notable difference in the grain morphology or dendritic microstructure was observed. Besides this temperature being below the dissolution temperature of the Laves phase, they remained visible in the interdendritic regions; see Fig. 3c. The primary objective of the DA treatment is to precipitate γ' and γ'' strengthening phases [18], some of its quantities may have precipitated in the matrix. As the DA temperature is not sufficient to dissolve Nb-rich Laves phases, a minimal quantity of γ' and γ'' strengthening phases was precipitated.

3.4 Microstructure in HSA condition

HSA treatment performed at 1080 °C completely recrystallized the microstructure. As this temperature exceeds the dissolution temperature of the Laves phase, neither Laves nor dendrites were observed; see Fig. 2g and 2h [39]. During the initial high temperature cycle of HSA treatment, the Nb released from the dissolution of Laves diffused back into the matrix and precipitated γ' and γ'' strengthening phases during the final DA cycle; see Fig. 4a. Fine acicular δ phase can be observed along the grain boundaries in (Fig. 4c) and some globular Nb-rich particles were identified inside the grains in Fig. 3d, which could be either δ phase or carbide. In addition, the annealing twins were detected in the HSA microstructure in Fig. 2h. The combination of recrystallized grains, dissolution of Laves phases, precipitation of γ' and γ'' strengthening phases, and appearance of annealing twins contributed to the highest performance of HSA treated TPMS structures. The annealing twins and acicular δ phase precipitated at the grain boundary act as a barrier to dislocation motion, improving the strength of the TPMS structure [46].

3.5 XRD pattern in AB and heat-treated conditions

Figure 5 illustrates the X-ray diffraction (XRD) pattern of In718 in AB, SR, DA, and HSA conditions. Prominent diffraction peaks of γ matrix are clearly visible. However, secondary precipitates including δ, γ' and γ'' were not detected due to their presence being lower than the detection limit of XRD. Moreover, diffraction peaks of γ' and γ'' overlap with the γ matrix peak due to coherency and cannot be

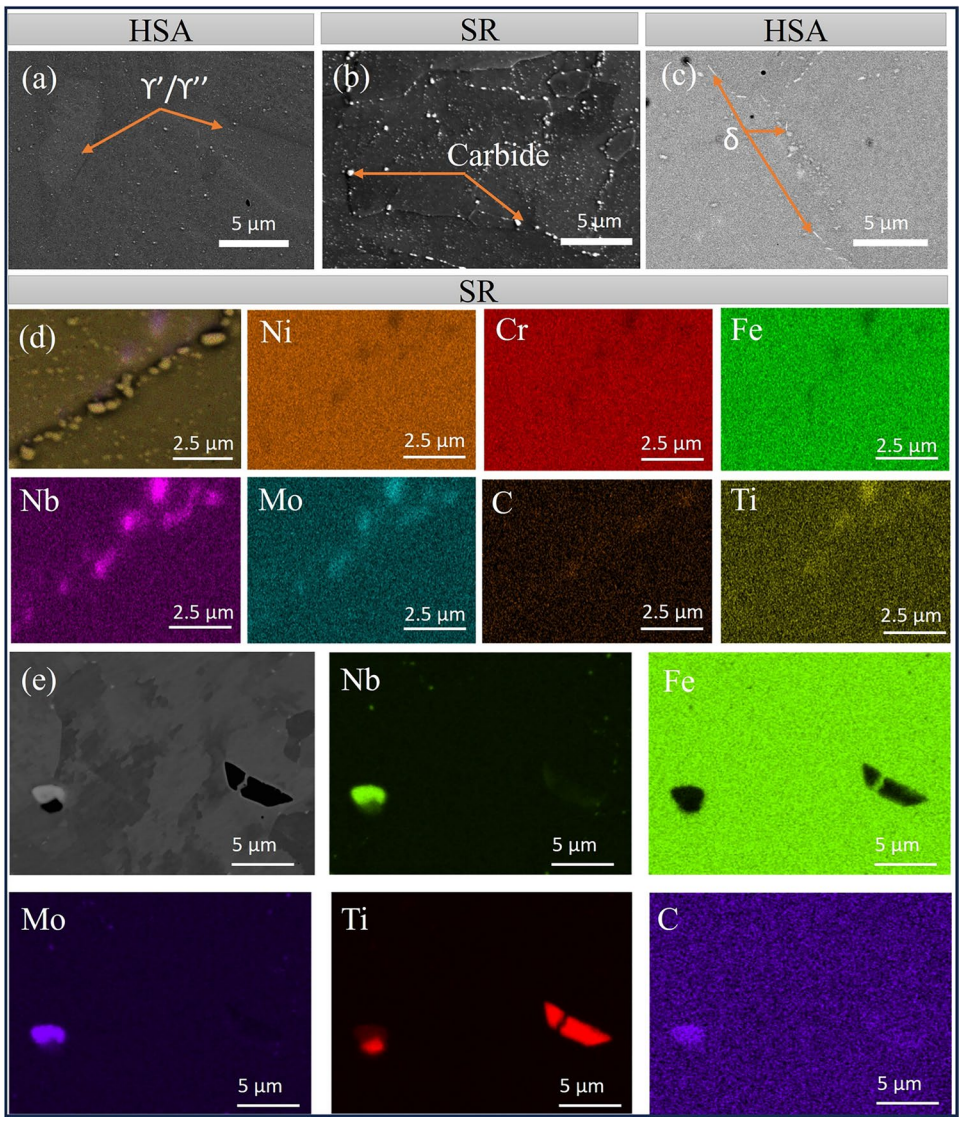

Fig. 4 Phases identified at different heat treatment conditions, **a** γ',γ'' phases in HSA treatment, **b** High volume of carbides in SR samples, **c** acicular δ phase at grain boundary, **d** EDS map diagram of Laves phases, **e** EDS map analysis of carbide precipitate

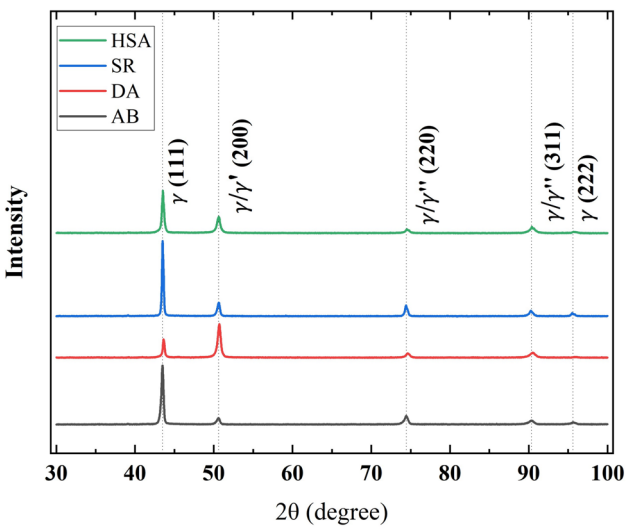

Fig. 5 XRD pattern of In718 in different conditions

distinguished [35]. A noticeable increase in the 2θ values of diffraction peaks can be observed in the case of DA samples. In the DA process, γ' and γ'' phases were precipitated, leading to the depletion of Nb, Al, and Ti elements from the γ matrix, which decreases interplanar spacing [47]. According to Bragg's law, a decrease in interplanar spacing causes a peak to appear at higher 2θ values.

In contrast, HAS-treated samples depict a slight decrease in 2θ values, which is caused by the dissolution of micro-segregation elements in the matrix during the high temperature dissolution cycle. Although the precipitation of γ' and γ'' phases during the final DA cycle increases the 2θ values, the prior dissolution of micro segregation elements reduces the final 2θ peak position. Similarly, for the SR sample, since only the partial dissolution of the micro-segregation of elements occurs without γ'/γ'' precipitation the location of peaks shifts to slightly lower 2θ values.

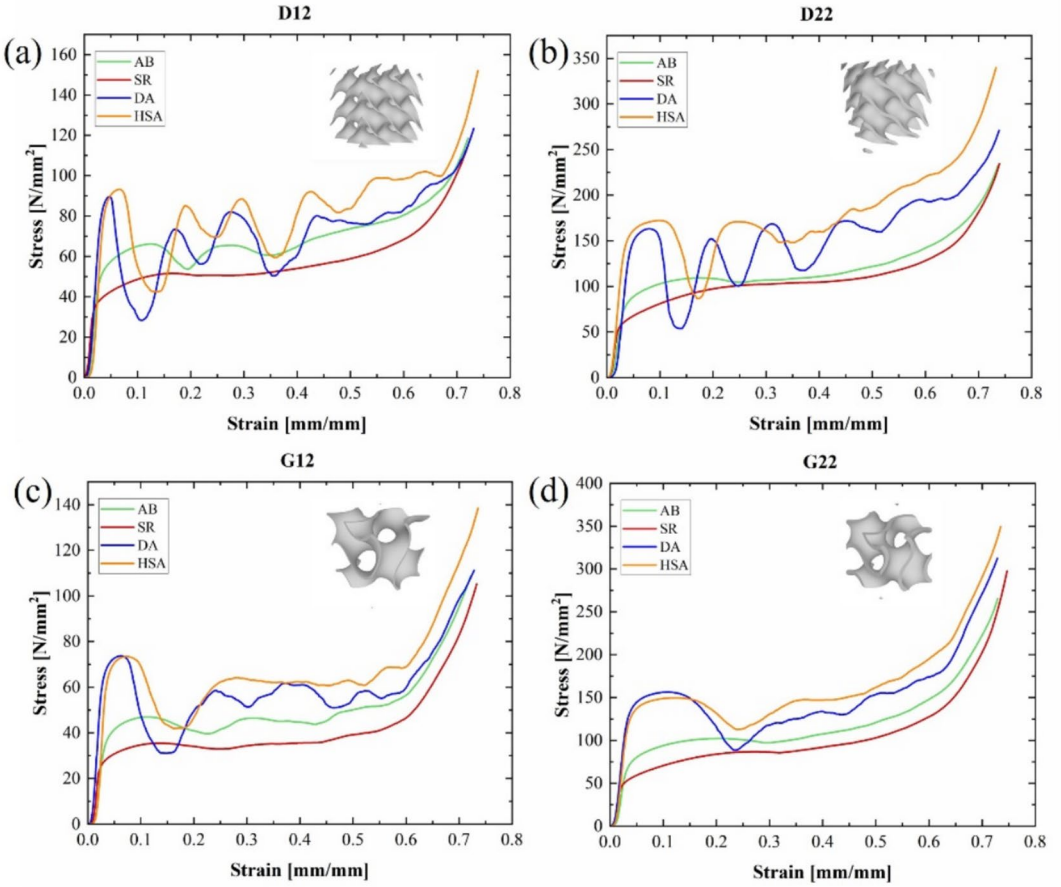

Fig. 6 Stress–strain response of TPMS structures in as built and heat-treated conditions for **a** D12, **b** D22, **c** G12, and **d** G22

3.6 Quasistatic compressive stress strain behaviour of TPMS structures

The stress–strain curves of the D12, D24, G12, and G24 TPMS structures for quasi-static compression test conditions are shown in Fig. 6. The stress strain response of TPMS structures initiates with an elastic–plastic deformation stage, leading to a stress plateau. During the plateau region, the TPMS absorbs very high applied energy. This region ends with the densification stage, where stresses rise rapidly owing to the closure of TPMS porosity. Similar behaviour of the stress–strain curve was also noted for the TPMS from Ti6Al4V in [48] and [49].

The stress strain response of AB TPMS structures was very stable, exhibiting only minor fluctuations. This stability is connected to their deformation behaviour, which involves layer by layer or collective collapse of layers. Amongst all TPMSs, stress strain behaviour of the SR TPMS structure was the most stable, owing to its uniform deformation behaviour, which shows no cracks or shear bands. The consistent stress–strain response of AB and SR TPMS structures indicates their bending dominated deformation behaviour, which is preferable for energy absorption devices in the aerospace and energy sectors.

In contrast, the stress strain response of HSA and DA TPMS structures suffered from a significant loss of strength immediately following the peak stress; see Fig. 6. This drop is primarily caused by the early formation of a single shear band, which later developed into double diagonal shear bands. Owing to topological differences, strength loss was more pronounced in the diamond TPMS and less obvious in the gyroid TPMS. The oscillations in stress level continued, corresponding to the sequential collapse of TPMS layers, indicating stretch dominated deformation behaviour in the DA and HSA TPMS structures.

3.7 Deformation behaviour of TPMS structures

Relative density, topology, and heat treatment impact the deformation and fracture behaviour of TPMS structures like their mechanical properties; see Fig. 7. The AB D12 TPMS structure deformed in a layer-by-layer sequence, initiated at the edges and progressed towards the centre with a

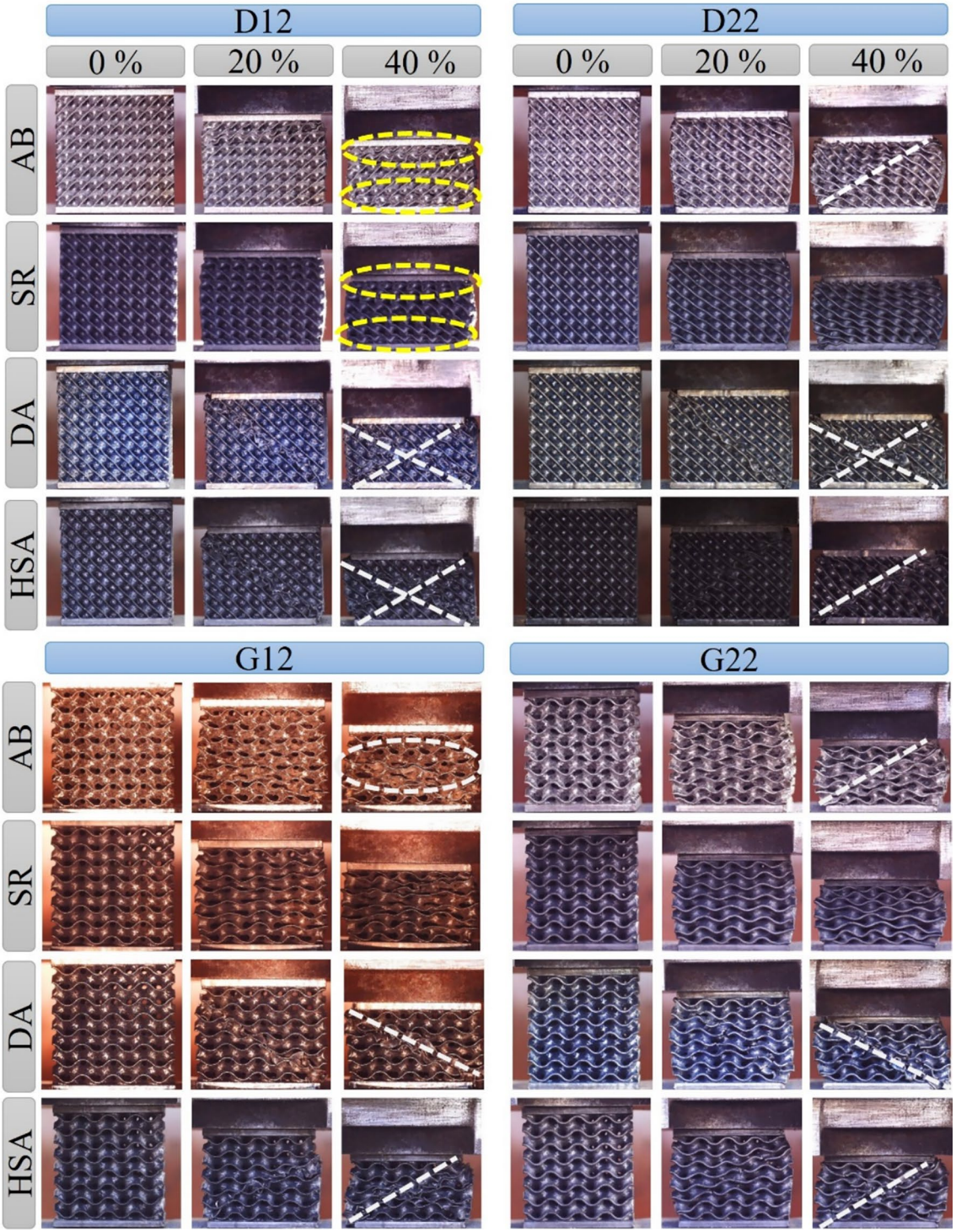

Fig. 7 Deformation behaviour of TPMS structures in as built and heat-treated conditions

very stable stress–strain response. This deformation mode is preferred due to its slower strength reduction, maximum energy absorption capacity till densification, and bending dominated deformation. Fracture behaviour of these TPMS structures in the AB state was mostly ductile and distributed in multiple layers, which caused a delayed and progressive failure mode.

Conversely, for D12 TPMS structures subjected to DA and HSA treatments, deformation started with a 45° shear zone, which dropped its strength significantly and advanced

to a double diagonal band. This change is attributed to the development of γ' and γ'' precipitates which increases the strength significantly by developing coherency strains and also act as dislocation pinning sites. However, these strengthening precipitates also lower ductility and foster premature shear banding. These precipitates also changed the deformation mode of D12 TPMS to stretch-dominated from bending dominated, and fracture behaviour becomes brittle in nature, which promotes sharper crack propagation. A similar kind of transformation in deformation mechanism was also observed in previous studies [50].

Topology plays a critical role in governing the impact of these precipitates on the deformation pattern. For instance, the smooth curvature and connectivity of gyroid TPMS distributed stress more uniformly and led to the formation of a single shear band even in the DA and HSA treatment conditions. However, D12 TPMS demonstrated double diagonal shear band formation due to its relatively sharp curvature, which deepened the impact of strengthening precipitates. High stresses in the diamond TPMS due to its sharp curvature in comparison to the gyroid TPMS were noted in the finite element modelling in previous studies [14, 51].

At higher relative density, the deformation behaviour of both TPMS has transformed, but its effect can only be observed in the AB state, could be due to the absence of notable precipitates. Notably, the SR TPMS has maintained its uniform deformation pattern even at higher relative density or any change in topology, most likely due to the absence of strengthening precipitates, which kept its plastic deformation behaviour.

3.8 Calculation of mechanical properties of TPMS structures

The mechanical properties of TPMS structures were investigated in detail from their stress–strain data in accordance with ISO 13314:2011 as follows:

Modulus of elasticity, E: slope of linear part of compression stress strain curve.

Yield strength, σ_y: from 0.2% offset method.

Compressive strength, σ_{max}: first local maximum on the stress–strain response of TPMS structures.

Plateau stress, σ_{pl}: the arithmetic mean of stresses in 20–40% strain range.

Furthermore, to compare the impact of heat treatment and relative density, the mechanical properties of TPMS structures were normalised with relative density, ρ and compared. The normalised mechanical properties were denoted by sign;$\sigma_y^*, \sigma_{pl}^*, \sigma_{max}^*$.

Table 6 Compressive mechanical properties of TPMS structures

Sample	Treatment method	Modulus of elasticity, E [MPa]	0.2% Yield strength, σ_y [MPa]	Compressive strength, σ_{max} [MPa]	Plateau stress, σ_{pl} [MPa]
D12	AB	3480.25	42.53	65.29	62.18
D12	SR	3403.45	32.43	50.95	51.20
D12	DA	4675.80	80.83	95.59	73.89
D12	HSA	4833.15	79.83	97.60	77.59
D22	AB	4484.90	67.60	109.10	106.35
D22	SR	4968.20	52.00	104.79	103.45
D22	DA	6611.30	132.6	167.75	136.41
D22	HSA	6820.65	130.24	169.40	158.26
G12	AB	2627.15	30.41	45.53	42.52
G12	SR	2828.20	23.90	36.55	35.24
G12	DA	3628.60	58.51	71.33	55.32
G12	HSA	3777.60	58.89	72.19	59.15
G22	AB	4166.60	60.66	99.89	98.58
G22	SR	4540.70	46.09	88.87	88.87
G22	DA	6271.80	117.58	156.22	115.05
G22	HSA	6195.20	112.22	149.30	131.55

3.9 Effect of heat treatment on mechanical properties of TPMS structures

Heat treatment significantly influences the mechanical properties of TPMS The mechanical properties of these structures were improved following heat treatment, except for the SR treated TPMS; see Fig. 6 and detailed in Table 6. Figure 8 illustrates the percentage improvements in mechanical properties of TPMS following the three heat treatments. Yield strength demonstrated the most enhancement, whilst the plateau stress has displayed the least sensitivity to heat treatment.

Amongst the heat treatments, the highest improvements were noted in DA and HSA treated samples. The best performance of HSA TPMS structures is primarily attributed to the dissolution of Laves phases and precipitation of γ' and γ'' strengthening phases. Although HSA composed of multiple cycles with three stages of heat treatment, whilst DA is only a single step, yet both of these treatments made comparable improvements in mechanical properties. Considering the extra steps and time involved, DA can replace HSA for best performance, time, and cost savings. Conversely, SR led to negative improvement in mechanical properties, which may be caused by high volumes of carbides identified in this condition; see Fig. 4b. A higher volume of carbides is detrimental to the mechanical properties of In718, which promotes crack formation and degrades mechanical properties, especially in compressive loading.

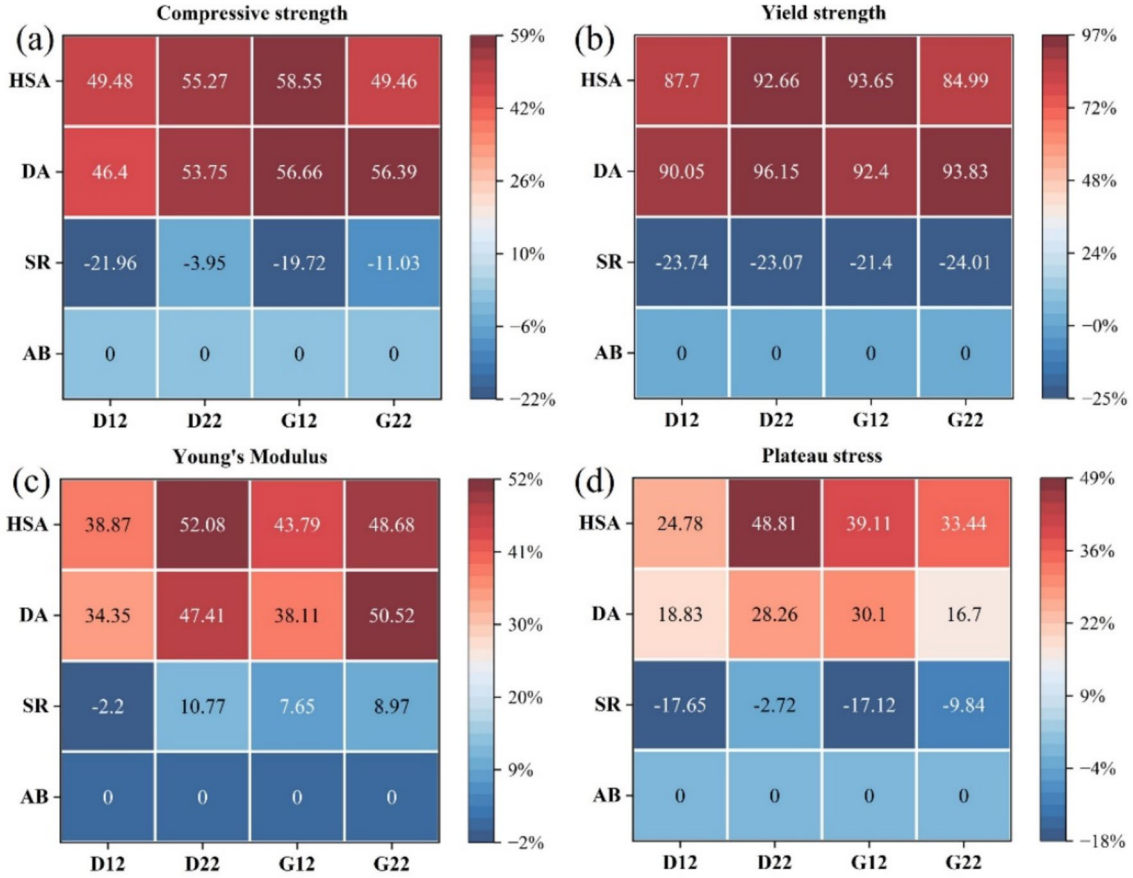

Fig. 8 Mechanical property improvement in terms of percentage for TPMS structures **a** compressive strength, **b** yield strength, **c** modulus of elasticity, and **d** plateau stress

3.10 Effect of relative density and topology on mechanical properties of TPMS structures.

The mechanical properties of TPMS structures vary with relative density and topology. Compressive strength of diamond TPMS at 22% relative density was 67% higher than diamond TPMS with 12% relative density. Similarly, the compressive strength of the gyroid at 22% relative density

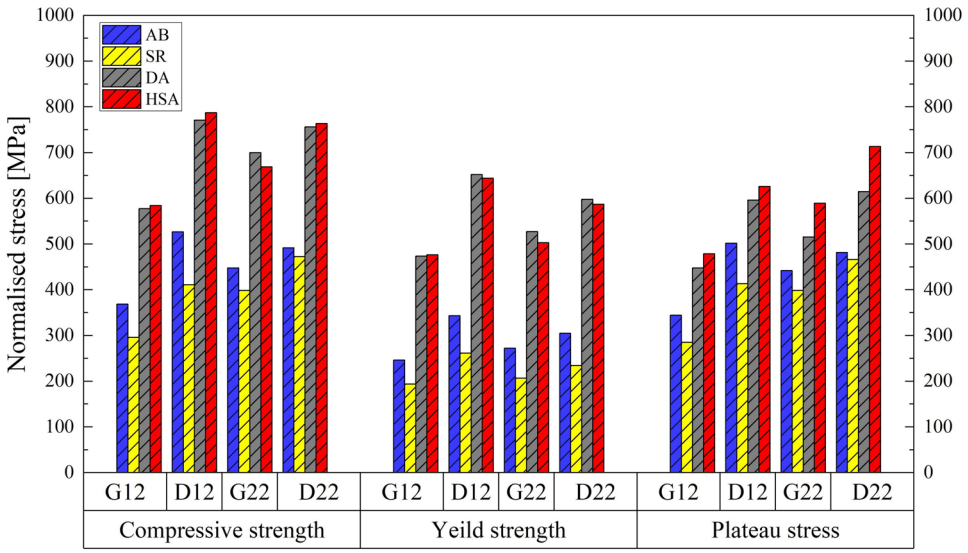

Fig. 9 Normalised mechanical properties of TPMS structures in as built and heat-treated condition

was 117% higher than its counterpart with 12% relative density. However, at 12% relative density, the compressive strength of diamond was 43.39% higher than gyroid. This supports the fact that, unlike bulk In718, the mechanical properties of the TPMS structures are strongly influenced by both topology and relative density. To further compare the impact of these parameters, the normalised mechanical properties are plotted in Fig. 9. The bar charts clearly demonstrate a notable difference in compressive strength, yield strength, and plateau stress as a function of relative density and topology. Notably, HSA and DA treated TPMS demonstrate high mechanical properties, and SR treated samples exhibit lowest property values.

4 Energy absorption behaviour of TPMS structures

4.1 Method for calculating energy absorption properties of TPMS structures

The energy absorbed, W per unit volume of TPMS structure, at strain ε is given by:

$$W = \int_0^{\varepsilon} \sigma(\varepsilon) d\varepsilon$$

This energy absorption is maximum at densification strain, ε_d.

Energy absorption efficiency, η: is the ratio of energy absorbed per unit volume to the corresponding stress and can be expressed as:

$$\eta = \frac{1}{\sigma(\varepsilon)} \int_0^{\varepsilon} \sigma(\varepsilon) d\varepsilon$$

An important parameter to measure the energy absorption according to 1S0 13,314:2011 is *ideality, W_i:*

$$W_i = \frac{W}{\sigma(\varepsilon) * \varepsilon}$$

where ε is total strain and $\sigma(\varepsilon)$ is corresponding stress.

The specific energy absorption (W_s), of the TPMS structures was also calculated from the energy absorption W with the following expression:

$$W_s = \frac{W}{m}$$

where, m is the mass of TPMS structure.

4.2 Energy absorption capacity (W) of TPMS structures

The energy absorption capacity and densification strain were improved following heat treatment in all TPMS structures, except for SR treated TPMS, as illustrated in Fig. 10 and detailed in Table 7. Despite exhibiting the most stable plateau region and bending dominated deformation, SR TPMS's plateau stress, W, and densification strain were the lowest amongst all heat-treated samples. In contrast, HSA and DA treated TPMS demonstrated high values of these properties, with only minor differences amongst them. These findings suggest that HSA and DA treated TPMS are suitable for high energy absorption and load bearing applications. However, the high energy absorption properties of HSA and DA treated TPMS—despite their stretch dominate behaviour are contradictory to previous studies, offering new insight into the positive impact of these treatments [12].

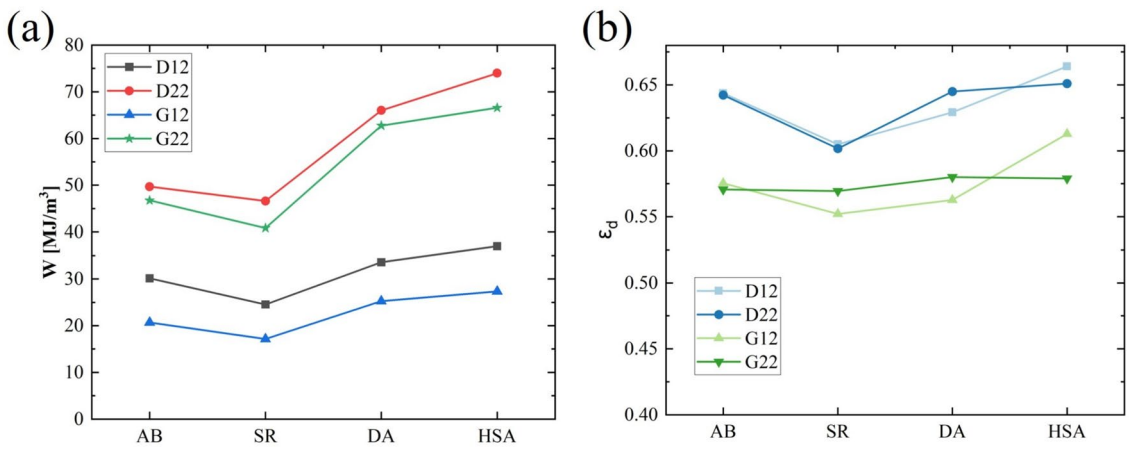

Fig. 10 **a** Energy absorption capacity of TPMS structures in different states and **b** Densification strain

Table 7 Energy absorption properties of TPMS structures

Sample	Treatment method	Energy absorption, $W_{50\%}$ [MJ/m^3]	Specific energy absorption, W_s [J/kg]$\times 10^{-3}$	Densification strain, ε_d	Energy Absorption efficiency,η
D12	AB	30.14	0.86	0.64	0.36
D12	SR	24.55	0.71	0.60	0.35
D12	DA	33.56	0.98	0.63	0.34
D12	HSA	37.02	1.06	0.66	0.37
D22	AB	49.68	1.14	0.64	0.34
D22	SR	46.61	1.04	0.60	0.33
D22	DA	66.02	1.50	0.64	0.33
D22	HSA	73.98	1.67	0.65	0.35
G12	AB	20.69	0.62	0.57	0.36
G12	SR	17.17	0.52	0.55	0.36
G12	DA	25.24	0.78	0.56	0.33
G12	HSA	27.33	0.83	0.61	0.34
G22	AB	46.74	1.06	0.57	0.34
G22	SR	40.83	0.91	0.57	0.32
G22	DA	62.75	1.42	0.58	0.35
G22	HSA	66.57	1.50	0.57	0.35

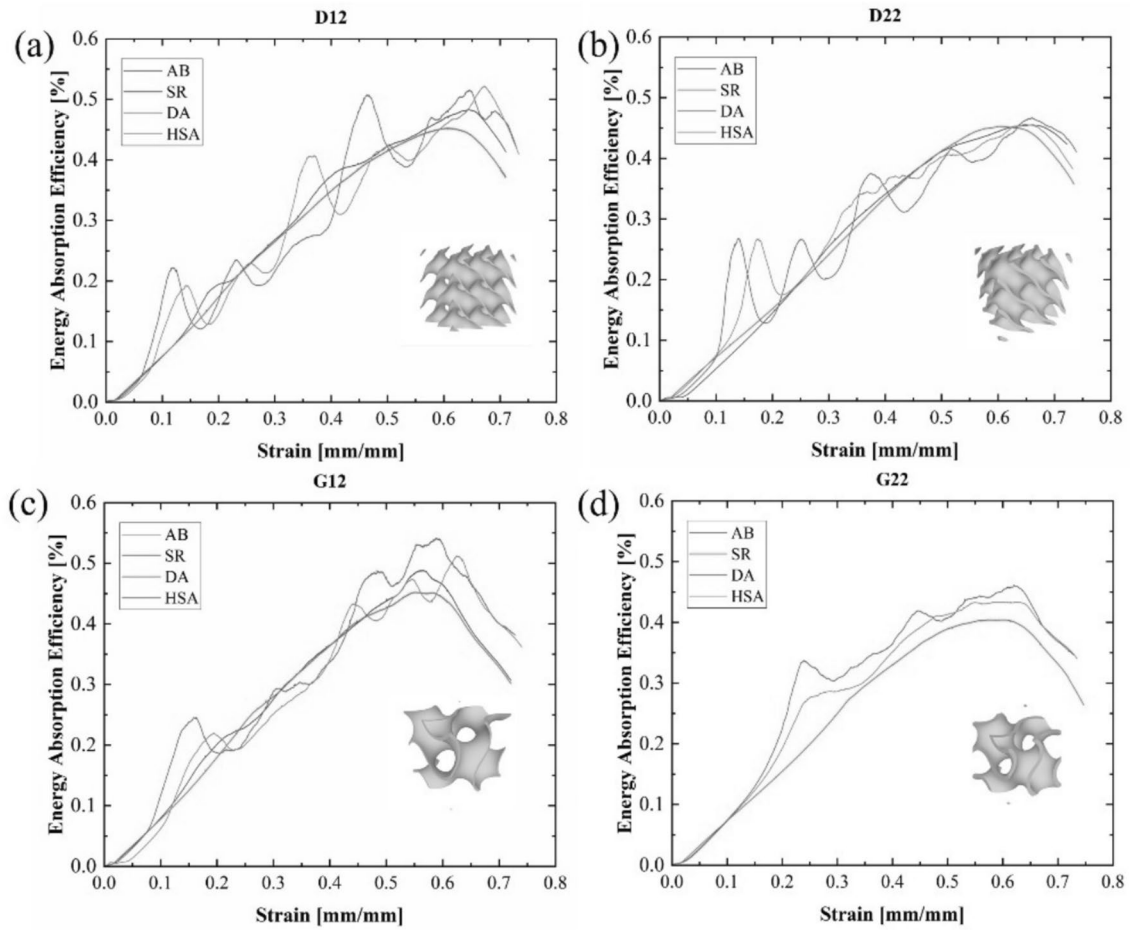

Fig. 11 Energy absorption efficiency of **a** D12, **b** D22, **c** G12, and **d** G22 TPMS structures

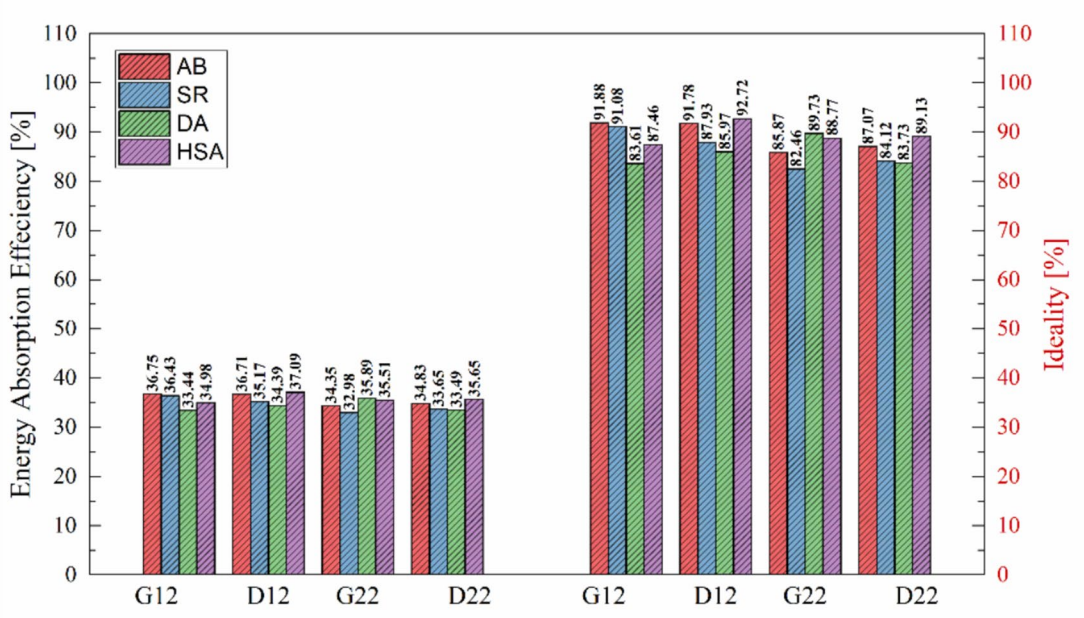

Fig. 12 Energy absorption efficiency (left) and Ideality (right) comparison of TPMS structures in different states

4.3 Energy absorption efficiency of TPMS structures in AB and heat-treated state

The η curve and its corresponding value at 40% strain are illustrated in Fig. 11 and Fig. 12, respectively. Ideality, which is the measure of how closely the energy absorption capacity of the TPMS structure approaches the ideal form, ranged between 82.46 and 92.72% in this study, illustrated in Fig. 12 [52]. From the beginning, η curve exhibited continuous increment until densification. Heat treatment has made some significant changes to the behaviour of η curve. η curve of SR and AB treated samples has demonstrated a quadratic rise in the beginning, followed by linear behaviour leading upto densification. The stability of the SR and AB η curves suggests their application for energy absorption requiring high stability.

In contrast, HSA and DA treated TPMS exhibited higher fluctuations in their η curve, attributed to their deformation behaviour and fluctuating stress levels observed in its plateau regions. Amongst all conditions, AB and HSA treated samples possess the highest energy absorption efficiency; see Fig. 12. However, energy absorption efficiency values did vary based on TPMS relative density or topology. In fact, the energy absorption efficiency was slightly reduced at a higher relative density.

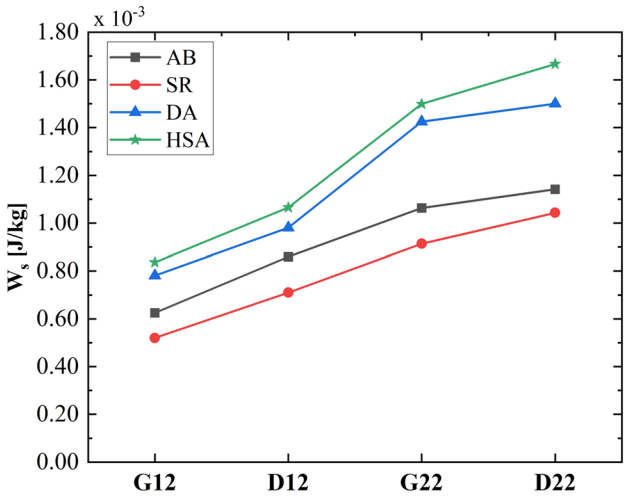

Fig. 13 W_s of TPMS structures in different states

4.4 Specific energy absorption (W_s) of TPMS structures

W_s Accurately measures the lattice structure's energy absorption capability. It serves as a strong indicator of the lattice's potential for energy absorption and is expressed as energy absorption capacity per unit mass. The W_s of the TPMS structure are tabulated in Table 7 and illustrated in Fig. 13. Notably, W_s showed substantial improvement in the DA and HSA treated samples; however, SR had a detrimental impact. The improvements in W_s after HSA treatments were 23.2%

for D12, 46.5% for D22, 33.8% for G12, and 41.5% for G22 TPMS structures. The positive impact of DA and HSA treatments was likely due to the precipitation of strengthening phases γ' and γ''. Overall, the improvements in W_s values emphasise the importance of heat treatment in improving TPMS's energy absorption properties.

5 Conclusion

This study investigated the effect of three heat treatments-SR, DA, and HSA on the mechanical behaviour of In718 TPMS structures. The heat treatments were chosen based on the recommendation from additive manufacturing heat treatment standards for In718 [53]. Whilst their influence on TPMS structures was not thoroughly explored. Previous studies have found a greater impact of HSA treatment on tensile strength of bulk In718 as compared to DA treatment [33]. However, in the current study, HSA and DA led to almost similar improvements in the mechanical properties under compression testing. Therefore, DA treatment is more promising for TPMS structures, considering the longer processing time, cost, and efforts in HSA treatment.

Although SR significantly improved the tensile strength of bulk In718, even comparable to HSA and DA treated samples [32], SR has shown a detrimental impact on the mechanical properties of TPMS structures in this study. Therefore, SR is not recommended to treat TPMS structures. Previous studies on In718 TPMS structures did not address the comparative effect of these three heat treatments [54, 55].

Additionally, these heat treatments have the potential for enabling In718 TPMS structures in complex internal components of cooling channels, aircraft engine parts, turbine blades, and other high temperature applications in corrosive environments. Given the challenges associated with machining In178 due to its high hardness, In718 TPMS structures can be easily manufactured via the SLM method. These TPMS structures are suited for applications requiring light weight, corrosion resistance, high heat dissipation, and high mechanical properties. However, in order to ensure industrial adaptability, optimised heat treatment needs to be applied based on the conclusion of this study.

6 Concluding remarks

This study investigated the impact of three standard heat treatments: stress-relieving, direct ageing, and homogenization solution ageing on the microstructure and mechanical behaviour of In718 TPMS structures. These key findings are as follows:

- **Microstructure**: the AB In718 showed micro-segregation, dendritic structures, and columnar grains aligned with the build direction. SR treatment led to partial recrystallization and partial dissolution of Laves, whilst HAS led to complete recrystallization and complete dissolution of Laves. Strengthening phases were precipitated only in DA and HSA treatments.
- **Mechanical behaviour**: HSA and DA treated TPMS showed stretch-dominated behaviour, improved compressive strength, modulus of elasticity, and yield strength. However, SR and AB TPMS showed bending dominated behaviour, inferior mechanical properties, but a smoother plateau region.
- **Energy absorption**: HSA and DA treated TPMS showed superior energy absorption properties and densification strain despite their stretch-dominated behaviour. This makes TPMS structure suitable for high load bearing and energy absorption applications, such as energy sector and aerospace applications. These results contradict previous studies and gives new insight into the impact of heat treatment on TPMS structures.
- **Stress relieving**: SR showed a positive impact on bulk In718; however, it was less effective for TPMS structures when investigated in this study. This behaviour can be attributed to high volumes of carbide formation after SR treatment, which makes SR less suitable for porous structures.

Additionally, by increasing relative density TPMS's mechanical properties were improved, and diamond TPMS outperformed gyroid TPMS in terms of mechanical strength.

7 Future perspective

The mechanical behaviour of TPMS structures was significantly altered by heat treatment. Both HSA and DA led to stretch dominated behaviour and improved energy absorption properties, but they introduced higher fluctuation in their stress strain response. In contrast, SR has led to bending dominated behaviour of TPMS with inferior mechanical properties. To address these issues, a modified heat treatment cycle based on DA or HSA treatment can be developed to provide higher strength, stiffness, and stable stress strain response whilst simultaneously improving the load bearing and energy absorption characteristics.

Acknowledgements The authors acknowledge the facilities, and the scientific and technical assistance, of the Microscopy Australia Facility at the Centre for Microscopy and Microanalysis (CMM), The University of Queensland and Griffith University.

Author contributions Mobin Majeed wrote the main manuscript text and prepared all tables and figures. Both authors reviewed the manuscript.

Funding Open Access funding enabled and organized by CAUL and its Member Institutions.

Data availability No datasets were generated or analysed during the current study.

Declarations

Conflict of interest The authors declare that there are no competing interests.

References

1. Ling C et al (2019) Mechanical behaviour of additively-manufactured polymeric octet-truss lattice structures under quasi-static and dynamic compressive loading. Mater Des 162:106–118
2. Maconachie T et al (2019) SLM lattice structures: properties, performance, applications and challenges. Mater Des 183:108137
3. Chen L-Y et al (2021) Additive manufacturing of metallic lattice structures: unconstrained design, accurate fabrication, fascinated performances, and challenges. Mater Sci Eng R Rep 146:100648
4. Feng J et al (2021) Isotropic porous structure design methods based on triply periodic minimal surfaces. Mater Des 210:110050
5. Majeed M et al (2022) Influence of post-processing on additively manufactured lattice structures. J Braz Soc Mech Sci Eng 44(9):389
6. Qiu N et al (2024) Experimental and numerical studies on mechanical properties of TPMS structures. Int J Mech Sci 261:108657
7. Wakjira Y, Cioni A, Lemu HG (2024) Current status of the application of additive-manufactured TPMS structure in bone tissue engineering. Progr Additive Manuf
8. Ravichander BB et al (2023) Mechanical and corrosion behavior of sheet-based 316L TPMS structures. Int J Mech Sci 254:108439
9. Khanna P et al (2024) Analysis of compression and energy absorption behaviour of SLM printed AlSi10Mg triply periodic minimal surface lattice structures. Structures. Elsevier
10. Gain AK, Cui Y, Zhang L (2024) Pore-gradient Ti6Al4V alloy mimicking the properties of human cortical bones: the design of TPMS structures by selective laser melting. Mater Sci Eng A 915:147220
11. Abdelaal AF et al (2023) Computational analysis of the compressive behavior of TPMS graded lattice structures versus primitive TPM lattice structures produced by additive manufacturing. In: ASME 2023 international mechanical engineering congress and exposition
12. Li Z et al (2023) Effect of heat treatment on compression properties of the 316L diamond structure fabricated through selective laser melting. J Market Res 25:5076–5095
13. Ahmed N, Barsoum I, Al-Rub RKA (2023) Numerical investigation of residual stresses in thin-walled additively manufactured structures from selective laser melting. Heliyon, 9(9)
14. Feng G et al (2023) Mechanical properties and deformation behavior of functionally graded TPMS structures under static and dynamic loading. Int J Impact Eng 176:104554
15. Xu L et al (2023) Effect of heat treatment on microstructures and mechanical properties of Inconel 718 additively manufactured using gradient laser power. Mater Sci Eng, A 868:144754
16. Kadam GS, Pawade RS (2022) Cutting force assessment in HSM of Inconel 718 aided with water vapour as an eco-friendly cutting fluid. In: Adjfkl A (ed) Recent advances in manufacturing processes and systems. Springer Nature Singapore, Singapore
17. Kadam GS, Pawade RS (2016) Sustainability modelling and assessment in high-speed turning of Inconel 718. Int J Precis Technol 6(3–4):249–261
18. Hosseini E, Popovich VA (2019) A review of mechanical properties of additively manufactured Inconel 718. Addit Manuf 30:100877
19. Wang X, Chou K (2019) The effects of stress relieving heat treatment on the microstructure and residual stress of Inconel 718 fabricated by laser metal powder bed fusion additive manufacturing process. J Manuf Process 48:154–163
20. Kadam GS, Pawade RS (2024) Water vapor cutting fluid assisted productive machining of Inconel 718. Mater Manuf Processes 39(1):98–109
21. Kadam GS, Pawade RS (2025) Innovative approaches to sustainable machining of Inconel 718 - exploring green metal working fluid alternatives and delivery strategies. J Adv Manuf Syst. https://doi.org/10.1142/S0219686726500095
22. Schröder J et al (2021) On the influence of heat treatment on microstructure and mechanical behavior of laser powder bed fused Inconel 718. Mater Sci Eng, A 805:140555
23. Schneider J et al (2022) Microstructure evolution in Inconel 718 produced by powder bed fusion additive manufacturing. J Manuf Mater Process 6(1):20
24. Zhang D et al (2015) Effect of standard heat treatment on the microstructure and mechanical properties of selective laser melting manufactured Inconel 718 superalloy. Mater Sci Eng, A 644:32–40
25. Wang X, Chou K (2017) Effects of thermal cycles on the microstructure evolution of Inconel 718 during selective laser melting process. Addit Manuf 18:1–14
26. Liu P et al (2019) Microstructural evolution and phase transformation of Inconel 718 alloys fabricated by selective laser melting under different heat treatment. J Manuf Process 39:226–232
27. Majeed M, Situ R, Javanbakht Z (2025) Effects of solution ageing in compressive behaviour of SLM-In718 triply periodic minimal surfaces. Progr Addit Manuf. https://doi.org/10.1007/s40964-025-01025-4
28. Huang W et al (2019) Heat treatment of Inconel 718 produced by selective laser melting: Microstructure and mechanical properties. Mater Sci Eng, A 750:98–107
29. Raghavan S et al (2017) Effect of different heat treatments on the microstructure and mechanical properties in selective laser melted INCONEL 718 alloy. Mater Manuf Processes 32(14):1588–1595
30. Popovich VA et al (2017) Impact of heat treatment on mechanical behaviour of Inconel 718 processed with tailored microstructure by selective laser melting. Mater Des 131:12–22

31. Zhao Y et al (2021) Impact of homogenization on microstructure-property relationships of Inconel 718 alloy prepared by laser powder bed fusion. Mater Sci Eng, A 826:141973
32. Babamiri BB et al (2020) Quantification of porosity and microstructure and their effect on quasi-static and dynamic behavior of additively manufactured Inconel 718. Addit Manuf 34:101380
33. Schneider J, Lund B, Fullen M (2018) Effect of heat treatment variations on the mechanical properties of Inconel 718 selective laser melted specimens. Addit Manuf 21:248–254
34. Zhao Y et al (2020) The effect of subsequent heat treatment on the evolution behavior of second phase particles and mechanical properties of the Inconel 718 superalloy manufactured by selective laser melting. Mater Sci Eng: A 794:139931
35. You X et al (2017) Effect of solution heat treatment on the precipitation behavior and strengthening mechanisms of electron beam smelted Inconel 718 superalloy. Mater Sci Eng, A 689:257–268
36. Yang H et al (2023) Microstructure, mechanical property and heat treatment schedule of the Inconel 718 manufactured by low and high power laser powder bed fusion. Mater Sci Eng A 863:144517
37. Madhusudhana Reddy G et al (2009) Improvement of mechanical properties of Inconel 718 electron beam welds—influence of welding techniques and postweld heat treatment. Int J Adv Manuf Technol 43(7):671–680
38. Gruber K et al (2021) Impact of high temperature stress relieving on final properties of Inconel 718 processed by laser powder bed fusion. Mater Sci Eng, A 813:141111
39. Wang W et al (2021) Process parameter optimization for selective laser melting of Inconel 718 superalloy and the effects of subsequent heat treatment on the microstructural evolution and mechanical properties. J Manuf Process 64:530–543
40. Deng D et al (2018) Microstructure and mechanical properties of Inconel 718 produced by selective laser melting: sample orientation dependence and effects of post heat treatments. Mater Sci Eng, A 713:294–306
41. Kadam G et al (2024) Design of rigid-locking variable-angular-span welding fixture. Eng Proc 66(1):35
42. Kadam GS et al (2023) Design of multi-angle welding fixture. Springer Nature Singapore, Singapore
43. Araujo LS et al (2021) The influence of the processing route on the fragmentation of (Nb,Ti)C stringers and its role on mechanical properties and hydrogen embrittlement of nickel based alloy 718. Int J Hydrogen Energy 46(29):16164–16178
44. Luo S et al (2019) Microstructural evolution and corrosion behaviors of Inconel 718 alloy produced by selective laser melting following different heat treatments. Addit Manuf 30:100875
45. Kwon SI et al (2016) Characterization of the microstructures and the cryogenic mechanical properties of electron beam welded Inconel 718. Metall and Mater Trans A 47(2):777–787
46. Shaw LL et al (2008) Strengthening via deformation twinning in a nickel alloy. Mater Sci Eng, A 480(1):75–83
47. Cao GH et al (2018) Investigations of γ', γ'' and δ precipitates in heat-treated Inconel 718 alloy fabricated by selective laser melting. Mater Charact 136:398–406
48. Fan X et al (2021) Design, mechanical properties and energy absorption capability of graded-thickness triply periodic minimal surface structures fabricated by selective laser melting. Int J Mech Sci 204:106586
49. Sun Q et al (2022) Compressive mechanical properties and energy absorption characteristics of SLM fabricated Ti6Al4V triply periodic minimal surface cellular structures. Mech Mater 166:104241
50. Nie Y et al (2023) Effect of heat treatment on mechanical properties, failure modes and energy absorption characteristics of lattice skeleton and sheet structures fabricated by SLM. J Market Res 26:4925–4941
51. EbrahimzadehDehaghani A et al (2025) Multifunctional design of triply periodic minimal surface structures for temporary pediatric fixation devices. Adv Eng Mater 27(11):2400518
52. Miltz J, Ramon O (1990) Energy absorption characteristics of polymeric foams used as cushioning materials. Polym Eng Sci 30(2):129–133
53. Gruber K et al (2022) Mechanical properties of Inconel 718 additively manufactured by laser powder bed fusion after industrial high-temperature heat treatment. J Manuf Process 73:642–659
54. Ahmed N, Barsoum I, Abu Al-Rub RK (2022) Numerical investigation on the effect of residual stresses on the effective mechanical properties of 3D-printed TPMS lattices. Metals 12(8):1344
55. Kyriakidis IF et al (2024) In situ investigation of tensile response for Inconel 718 micro-architected materials fabricated by selective laser melting. Materials 17(17):4433